"If I had only known, I would have been a locksmith."

ALBERT EINSTEIN

2

A comparison of the jet acceleration mechanisms in young stellar objects and active galactic nuclei

2.1 Introduction

Astrophysical jets were first discovered when Curtis (1918) observed a 'curious straight ray' emanating from the nucleus of the M87 nebula. Such jets are now commonly observed in a wide variety of astrophysical environments, including Active Galactic Nuclei (AGN), Young Stellar Objects (YSOs), stellar and compact binary systems and their presence is even inferred in the violent supernovae which manifest as Gamma-Ray Bursts. Despite an ever-growing mountain of observations[1], many of the fundamental questions regarding the basic processes which govern their acceleration and high degree of collimation over substantial length scales remain a mystery.

Since the relativistic AGN jets were discovered first, presumably powered by accretion onto the central black hole (Rees, 1984), it was natural that early models for jet formation were inherently relativistic (Ferrari, 1998). For example, the oft-cited mechanism of Blandford and Znajek (1977) involves tapping the rotational energy of a spinning black hole. The mere existence of jets in classes of object where black holes are not present clearly indicates that such processes cannot provide a universal explanation of jet origins. Similarly, mechanisms invoking a star rotating at near break-up speed (Shu et al., 1988) or accretion disc boundary layers (Pringle, 1989) must also be excluded (although in the latter case there may be some analogy in black hole accretion discs), unless we argue that different processes operate in each separate class of object, despite the ubiquity of jet production. Since it was clear from the lack of substantial thermal emission that the jet acceleration process was not purely hydrodynamic in nature (see e.g. Blandford and Rees, 1974; Konigl, 1982), nearly all jet production mechansisms invoke some kind of magnetic field, whether large- (Blandford and Payne, 1982; Pudritz and Norman, 1986) or small-

[1] for example a search of the NASA ADS for papers with 'jet' in the title produces 390 hits for 2003 alone.

(Heinz and Begelman, 2000) scale. Of these the most popular and by far the most successful mechanism for explaining both the acceleration and collimation of jets is the magneto-centrifugal model of Blandford and Payne (1982) which has been demonstrated in a number of numerical simulations (Ouyed and Pudritz 1997, 1999; Ouyed et al. 1997; Kudoh et al. 1998; Koide et al. 2000).

In this model a large scale vertical field threading the accretion disc causes material to be centrifugally accelerated along the magnetic field lines, analogous to 'beads on wires'. Blandford and Payne (1982) demonstrated that such acceleration could take place if the angle of inclination between the field lines and the disk was $> 30^{\circ}$. Although it might be claimed that some form of consensus has been reached on magnetocentrifugal acceleration forming the the heart of the jet production process, these models suffer from several problems. The first of these is the origin of the large-scale field which must be invoked for the model to work, in particular whether such fields can be either advected inwards from the environment from which the disc formed (see Lubow et al., 1994) or produced spontaneously from a dynamo operating in the disc itself (Tout and Pringle, 1992, 1996). The second problem is that large-scale magnetic fields dominated by toroidal components are found to be unstable (Spruit et al., 1997; Lucek and Bell, 1996; Begelman, 1998) (where the instabilities are similar to those observed in a wound-up rubber band, which begins to bend and kink as it becomes dominated by toroidal stresses). For this reason the role of collimation is now generally assigned to a dominant poloidal component of the field (e.g. Lucek and Bell 1997).

A further problem, and the issue we focus on in the present work, is that the Blandford and Payne (1982) model is scale-free (ie. self-similar). The problem with this is the fairly general observation that jet velocities appear to be very close to the escape velocity from the central gravitating object (Livio, 1999), suggesting that jets are somehow aware of the strength of the gravitational potential close to the central object itself. This would seem to indicate that the jet originates from the inner part of the accretion disc (ie. close to the central object) and is supported by observations such as those of HH30 showing a jet clearly emanating from the centre of the accretion disc (Burrows et al., 1996) and variability in the $\mu-$quasar system GRS1915+105, where dips in the X-ray flux are observed immediately prior to the observation of a blob of plasma being ejected into the jet, interpreted as the inner edge of the accretion disc dropping away prior to the ejection event (Mirabel et al., 1998; Mirabel and Rodríguez, 1999). Similar observations have been made over longer timescales in the active galaxy 3C120 by Marscher et al. (2002). Intrinsic jet velocities in both relativistic and non-relativistic jets are somewhat difficult to measure because in order to be visible the jet material must be interacting with the surrounding medium in some way (and therefore decelerating). In the YSO case, jet velocities are typically inferred from measurements of the proper motions of features travelling along the jet (such as the Herbig-Haro objects which are interpreted as shocks within the jet due to material travelling at different speeds) or by mapping the velocity structure around such features (Reipurth and Bally, 2001). Typical jet velocities thus measured lie in the range $v_{jet} \sim 300-500$ km/s (Eislöffel and Mundt 1998; Micono et al. 1998; Bally et al. 2001; Hartigan et al. 2001; Reipurth et al. 2002; Bally et al. 2002; Pyo et al. 2002) which may be compared to the escape velocity from a typical young star (mass 1 $M_{\odot}$, radius 5 $R_{\odot}$; Tout et al. 1999) of $v_{esc} \sim 270$ km/s. In the AGN case, jet velocities are observed to be very close to the speed of light, in keeping with the escape velocity from the central black hole. Although estimates vary, observationally typical Lorentz factors for AGN jets lie in the range $\gamma_{jet} \sim 5-10$ (Urry and Padovani 1995; Biretta et al. 1999), although arguments for higher values ($\gamma_{jet} \sim 10-20$) have been made on theoretical grounds

(Ghisellini and Celotti, 2001).

In recent years it has been suggested that small scale, tangled magnetic fields could perhaps both accelerate (Heinz and Begelman, 2000) and collimate (Li, 2002) jets, without invoking any large-scale field. These ideas are attractive theoretically as they are in keeping with the turbulent magnetic fields known to drive accretion in discs via the magneto-rotational instability (Balbus and Hawley, 1991). Collimation via small scale fields does not suffer from the problem of instabilities and since acceleration via small scale fields is an inherently local process, the scale associated with the acceleration regions would be naturally reflected in the velocity of the resulting outflow.

In this chapter we take an extremely simplified approach to the problem of jet acceleration, paying particular attention to the observation that jet velocities are of order the escape velocity from the central object. We pose the question of whether or not a simple scaling exists between jets accelerated in non-relativistic environments and those accelerated in relativistic environments by considering a highly simplified model of the jet acceleration process. Since we are concerned only with acceleration, not collimation, we examine the driving of a spherically symmetric outflow by injecting energy into an initially hydrostatic gas reservoir at a fixed radius close to the central object. The gas is treated in a simple manner as having a purely thermal pressure, P, and internal energy, u, and a ratio of specific heats γ which we take to be $\gamma = 4/3$. The exact value of γ is not particularly critical to the arguments developed in this chapter, provided that $\gamma < 5/3$ so that the outflow becomes supersonic. Taking $\gamma = 4/3$, however, is in fact appropriate to the case of an optically thick radiation-pressure dominated flow, and to the case in which the dominant pressure within the gas is caused by a tangled magnetic field (Heinz and Begelman, 2000). It should therefore, despite the simplistic treatment, allow us to draw some quite general conclusions.

If the same acceleration process is at work in both relativistic and non-relativistic jets, then the same (appropriately scaled) energy input rate should account for the observed jet velocities in both classes of object. Specifically, the energy input rate required to give rise to a final jet velocity $v_{jet} \sim 2v_{esc}$ in the non-relativistic case should also be able to produce outflows with Lorentz factors of $\gamma_{jet} \sim 7$ in the relativistic case. We therefore undertake the following computations: In §2.2 we examine the non-relativistic case, appropriate to YSO jets. Energy is injected at a steady rate over a small volume into an initially hydrostatic gas reservoir, following the time evolution of the gas as it expands. Since we cannot follow the time evolution for an infinite time, once the gas has reached a large enough radius the time-dependent solution is matched to a steady state wind solution in order to determine the terminal velocity of the outflow. In §2.3 exactly the same computations are performed using relativistic fluid dynamics, appropriate to AGN (and $\mu-$quasar) jets. The final jet velocity is then plotted as a function of the (dimensionless) energy input rate (heating rate) in both the relativistic and non-relativistic cases. Results and conclusions are presented in §2.4.

2.2 Non-relativistic (YSO) jets

2.2.1 Fluid equations

For YSO jets we expect the gravitational field to be well approximated by a non-relativistic (Newtonian) description. In one (radial) dimension the equations describing such a fluid including the effects of

energy input are expressed by the conservation of mass,

$$\frac{\partial \rho}{\partial t} + \mathrm{v}^r \frac{\partial \rho}{\partial r} + \frac{\rho}{r^2}\frac{\partial}{\partial r}(r^2 \mathrm{v}^r) = 0, \tag{2.1}$$

momentum,

$$\frac{\partial \mathrm{v}^r}{\partial t} + \mathrm{v}^r \frac{\partial \mathrm{v}^r}{\partial r} + \frac{1}{\rho}\frac{\partial P}{\partial r} + \frac{GM}{r^2} = 0, \tag{2.2}$$

and energy,

$$\frac{\partial (\rho u)}{\partial t} + \mathrm{v}^r \frac{\partial (\rho u)}{\partial r} + \left[\frac{P+\rho u}{r^2}\right]\frac{\partial}{\partial r}(r^2 \mathrm{v}^r) = \rho \Lambda, \tag{2.3}$$

where ρ, v^r, P and u are the fluid density, radial velocity, pressure and internal energy per unit mass respectively, M is the mass of the gravitating object (in this case the central star), and

$$\Lambda = \frac{dQ}{dt} = T\frac{ds}{dt} \tag{2.4}$$

is the heat energy input per unit mass per unit time (where T and s are the temperature and specific entropy respectively). The equation set is closed by the equation of state for a perfect gas in the form

$$P = (\gamma - 1)\rho u. \tag{2.5}$$

Scaling

To solve (2.1)-(2.5) numerically we scale the variables in terms of a typical length, mass and timescale. These we choose to be the inner radius of the gas reservoir $[L] = R_*$, the mass of the gravitating body $[M] = M_*$ and the dynamical timescale at the the inner radius ($r = R_*$), $[\tau] = (GM_*/R_*^3)^{-1/2}$. In these units $GM = 1$ and the density, pressure, velocity and internal energy, respectively, have units of density, $[\rho] = M_*/R_*^3$, pressure, $[P] = M_*/(R_*\tau^2)$, circular velocity at R_*, $[\mathrm{v}] = \sqrt{GM_*/R_*}$ and gravitational potential energy at R_*, $[u] = GM_*/R_*$. Note that the net heating rate per unit mass Λ is therefore given in units of gravitational potential energy, GM_*/R_*, per dynamical timescale at R_*, $(GM_*/R_*^3)^{-1/2}$. We point out that this scaling is simply to ensure that the numerical solution is of order unity and that when comparing the results to the relativistic simulations we scale the solution in terms of dimensionless variables.

2.2.2 Numerical solution

We solve (2.1)-(2.5) in a physically intuitive way using a staggered grid where the fluid velocity is defined on the half grid points whereas the density, pressure, internal energy and heating rate are specified on the integer points. This allows for physically appropriate boundary conditions and allows us to treat the different terms in a physical way by applying upwind differencing to the advective terms but using centred differencing on the gradient terms. The scheme is summarised in Figure 2.1 with the discretized form of the equations given in appendix A. The staggered grid means that only three boundary conditions

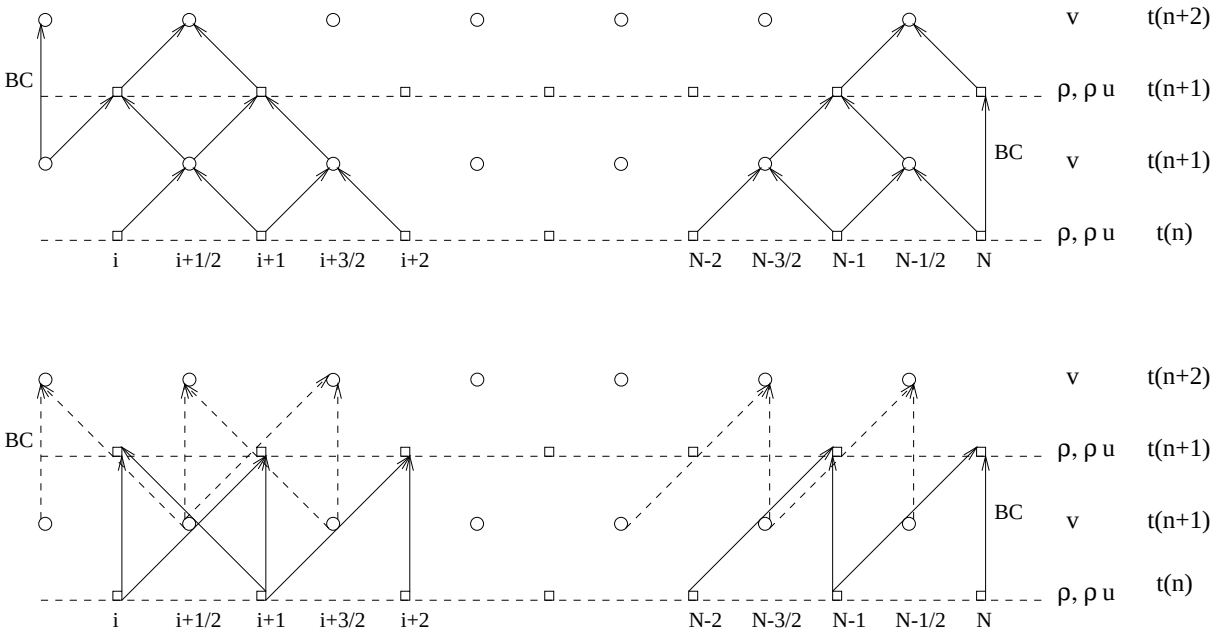

Figure 2.1: Schematic diagram of numerical method: density and internal energy are defined on the integer points while velocity is calculated on the half points. The solution requires one inner boundary condition on v and two outer boundary conditions for ρ and ρu. Updated velocities (v^{n+1}) are used to calculate ρ^{n+1} and ρu^{n+1}. The scheme allows centred differencing on terms involving staggered quantities (top panel) while upwind differencing is used on the advective terms (bottom panel).

are required, as shown in Figure 2.1. We set $v = 0$ at the inner boundary and the density and internal energy equal to their initial values (effectively zero) at the outer boundary.

2.2.3 Initial conditions

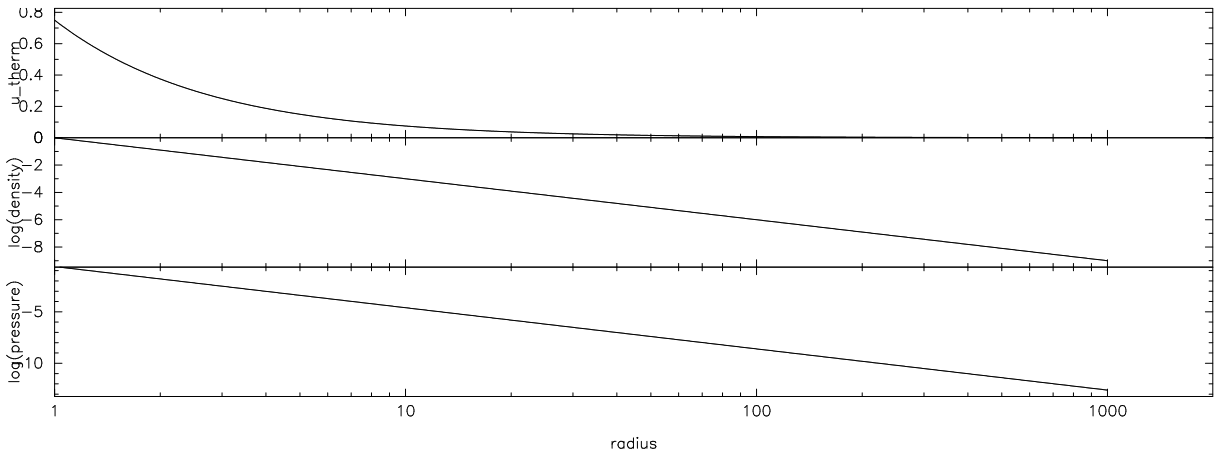

Figure 2.2: The initial conditions for the non-relativistic case, We plot profiles of density, pressure and internal energy per unit mass (or temperature) as functions of radius. The quantities here are dimensionless and the units are as described in §2.2.1.

The form of the initial conditions is not particularly crucial to the problem, as the wind eventually reaches a quasi-steady state that is independent of the initial setup. What the initial conditions do affect

is the time taken to reach this steady state (by determining how much mass must initially be heated in the wind). We proceed by setting up a body of gas (loosely 'an atmosphere') above the 'star' (or rather, an unspecified source of gravity) initially in hydrostatic equilibrium, such that v = 0 everywhere and

$$\frac{dP}{dr} = -\frac{GM\rho}{r^2}. \tag{2.6}$$

The pressure is related to the density by a polytropic equation of state

$$P = K\rho^{\gamma}, \tag{2.7}$$

where K is some constant. Combining these two conditions we obtain an equation for the density gradient as a function of radius

$$\frac{d\rho(r)}{dr} = -\frac{\rho(r)^{-(\gamma-2)}}{\gamma K}\frac{GM}{r^2}. \tag{2.8}$$

Integrating this equation from r to some upper bound R_∞ we obtain

$$\rho(r) = \left[\frac{\gamma-1}{\gamma K}\left(\frac{GM}{r} - \frac{GM}{R_\infty}\right)\right]^{1/(\gamma-1)}. \tag{2.9}$$

To ensure that pressure and density are finite everywhere (for numerical stability) we set $R_\infty = \infty$. The density is then given as a simple function of radius where it remains to specify the polytropic constant K. In scaled units we choose $K = (\gamma-1)/\gamma$ such that $\rho(R_*) = 1$ (*i.e.* the central density equals the mean density of the gravitating body – note that we neglect the self-gravity of the gas itself. Choosing K effectively determines the amount of mass present in the atmosphere and thus the strength of the shock front which propagates into the ambient medium (in terms of how much mass is swept up by this front).

We set the initial pressure distribution using (2.7). If we do this, however, the slight numerical imbalance of pressure and gravity results in a small spurious response in the initial conditions if we evolve the equations with zero heating. In the non-relativistic case the spurious velocity is kept to an acceptably small level by the use of a logarithmic radial grid (thus increasing the resolution in the inner regions). In the relativistic case however this slight departure from numerical hydrostatic equilibrium is more significant. This response is therefore eliminated by solving for the pressure gradient numerically using the same differencing that is contained in the evolution scheme. That is we solve from the outer boundary condition $P(r_{\max}) = K\rho(r_{\max})^{\gamma}$ according to

$$P_{i-1} = P_i - (r_i - r_{i-1})\frac{\rho_{i-1/2}}{r^2_{i-1/2}}. \tag{2.10}$$

Solving for the pressure in this manner reduces any spurious response in the initial conditions to below round–off error. The internal energy is then given from (2.5). The pressure calculated using (2.10) is essentially indistinguishable from that found using (2.7)($\Delta P/P \sim 10^{-5}$). The initial conditions calculated using equation (2.9), (2.10) and (2.5) are shown in Figure 2.2. We use a logarithmic grid with 1001 radial grid points, setting the outer boundary at $r/R_* = 10^3$. Using a higher spatial resolution does not affect the simulation results.

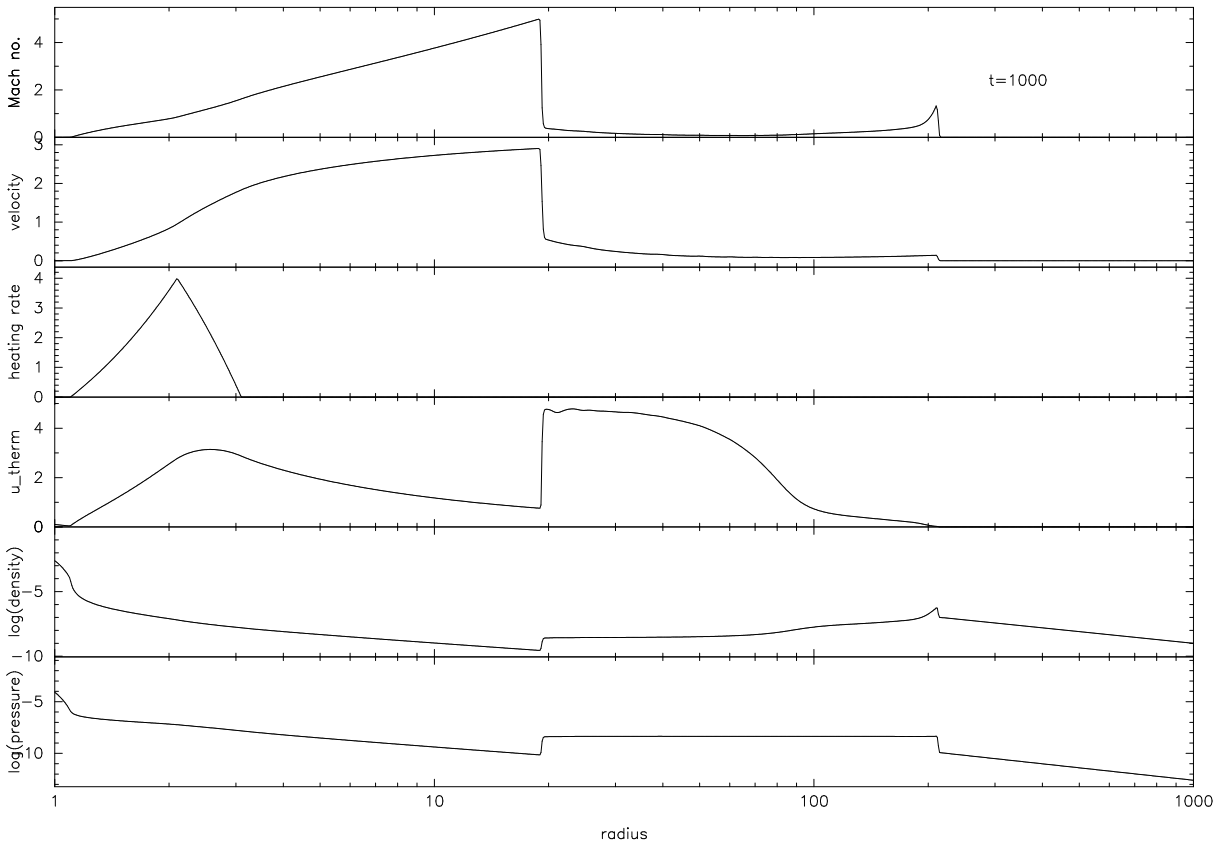

Figure 2.3: Results of a typical non-relativistic simulation at time $t = 1000$ (where units of time are the dynamical time at the innermost radius, $\sqrt{R_*^3/GM}$). Quantities shown are the Mach number (v/c_s), velocity, heating rate (Λ), internal energy per unit mass ($u \equiv u_{\rm therm}$), log(density) and log(pressure).

Heating profile

The choice of the shape of the heating profile $\Lambda(r)$ is fairly arbitrary since we wish simply to make a comparison between the non-relativistic and relativistic results. We choose to heat the wind in a spherical shell of a fixed width using a linearly increasing and then decreasing heating rate, symmetric about some heating radius $r_{\rm heat}$ which we place at $r = 2.1R_*$. The heating profile is spread over a radial zone of width $2R_*$ (that is the heating zone extends from $r = 1.1R_*$ to $3.1R_*$)(see Figure 2.3). We choose a heating profile of this form such that it is narrow enough to be associated with a particular radius of heating (necessary since we are looking for scaling laws) whilst being wide enough to avoid the need for high spatial resolution or complicated algorithms (necessary if the heat input zone is too narrow). The important parameter is thus the *location* of the heating with respect to the Schwarzschild radius, so long as the heating profiles are the same in both the relativistic and non-relativistic cases. Provided that the heating profile is narrow enough to be associated with a particular radius and wide enough to avoid numerical problems, the results do not depend on the actual shape of the profile used.

2.2.4 Results

The results of a typical non-relativistic simulation with a moderate heating rate are shown in Figure 2.3 at $t = 1000$ (where t has units of the dynamical time at the inner radius). We observe the effect of the heating propagating outwards in the atmosphere in the form of a shock front. After several hundred dynamical

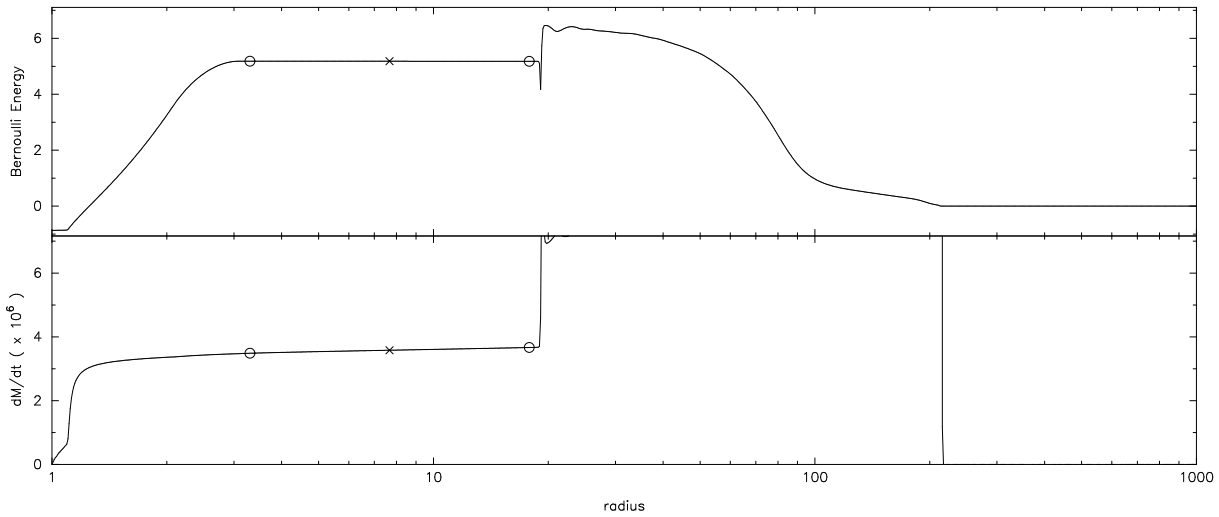

Figure 2.4: Bernoulli energy $E = \frac{1}{2}\mathrm{v}^2 + \rho u + P - GM/r$ (top) and mass outflow rate $\dot{M} = 4\pi r^2 \rho \mathrm{v}$ (bottom) in the time-dependent wind solution at $t = 1000$. The profiles are approximately constant over the region between the two circles. The sample point used to match this flow to the appropriate steady state solution is indicated by a cross.

times the wind structure approaches a steady state in that there is only a small change of the overall wind structure due to the shock continuing to propagate outwards into the surrounding medium. The small disturbance propagating well ahead of the main shock is a transient resulting from the response of the atmosphere to the instantaneous switch-on of the heating. The velocity of the gas begins to asymptote to a constant value as the shock propagates outwards. Plotting the mass outflow rate $\dot{M} = 4\pi r^2 \rho \mathrm{v}$ and the Bernoulli energy $E = \frac{1}{2}\mathrm{v}^2 + \rho u + P - GM/r$ as a function of radius (Figure 2.4), we see that indeed the wind structure is eventually close to that of a steady wind above the heating zone (ie. $\dot{M}$ and $E \sim$ constant). It is thus computationally inefficient and impractical to compute the time-dependent solution for long enough to determine an accurate velocity as $r \to \infty$ when the wind will continue to have a steady structure. Instead we find the steady wind solution for a given amount of energy input to the wind corresponding to the energy plotted in Figure 2.4 (top panel).

2.2.5 Steady wind solution

Non-relativistic, steady state ($\partial/\partial t = 0$) winds with energy input have been well studied by many authors, and the equations describing them can be found in Lamers and Cassinelli (1999), who credit the original work to Holzer and Axford (1970). The reader is thus referred to Lamers and Cassinelli (1999) for details of the derivation. As in the usual Bondi/Parker (Bondi 1952, Parker 1958) wind solution with no heat input, we set $\partial/\partial t = 0$ in (2.1)-(2.5) and combine these equations into one equation for the Mach number $M^2 = \mathrm{v}^2/c_s^2$ as a function of radius, given by

$$\frac{dM^2}{dr} = -\frac{M^2(2+(\gamma-1)M^2)}{2(M^2-1)\left[e(r)+GM/r\right]}\left[(1+M^2\gamma)\frac{dQ}{dr} + \frac{GM}{r^2}\frac{(5-3\gamma)}{(\gamma-1)} - \frac{4e(r)}{r}\right], \tag{2.11}$$

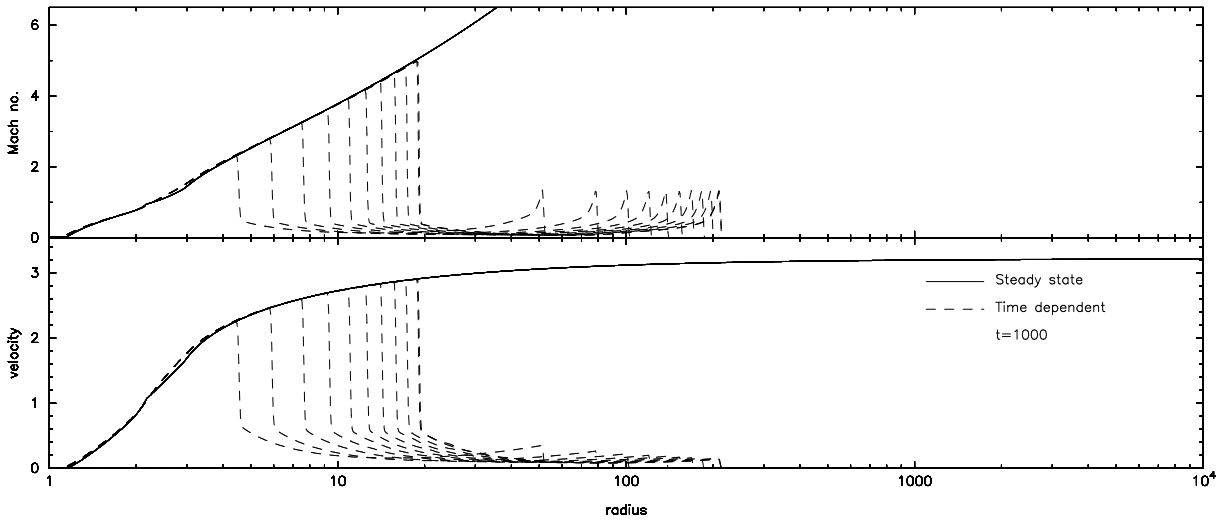

Figure 2.5: Steady wind Mach number (top panel) and velocity (centre panel) profiles are compared to the time-dependent solution (plotted every 100 dynamical times). There is a small discrepancy between the two solutions where we have taken the limit in approaching the singular point at $M = 1$, but an otherwise excellent agreement between the two solutions.

where dQ/dr is the local heating gradient and $e(r)$ is the Bernoulli energy which is specified by integrating the Bernoulli equation

$$\frac{de(r)}{dr} = \frac{d}{dr}\left[\frac{1}{2}\mathrm{v}^2 + \rho u + P - \frac{GM}{r}\right] = \frac{dQ}{dr}, \tag{2.12}$$

to give

$$\begin{aligned} e(r) &= e(r_\infty) - Q(r) \\ &= e(r_\infty) - \int_r^{r_\infty} \frac{dQ}{dr}, \end{aligned} \tag{2.13}$$

where $Q(r)$ is the total energy input to the wind. Since we are interested in the terminal velocity of the outflow we choose a point above the heating shell where the energy has reached its steady state value (*i.e.* where the energy is constant in Figure 2.4, top panel) and integrate outwards using the energy and Mach number at this point to solve (2.11) as an initial value problem. Note that in fact the terminal velocity is determined by the (constant) value of the Bernoulli energy above the heating zone since as $r \to \infty$, $e(r) \to \frac{1}{2}\mathrm{v}^2$. However we compute the steady wind profiles both inwards and outwards to show the consistency between the time-dependent solution and the steady state version.

In order to perform the inward integration, we must determine the energy at every point for our steady solution by subtracting the heat input from the steady state energy as we integrate inwards through the heating shell (2.13). To determine this however we must also determine the local (steady state) heating gradient dQ/dr, which is related to the (time dependent) heating rate Λ by setting $\partial/\partial t = 0$ in the time dependent version, ie.

$$\Lambda = \frac{dQ}{dt} = \frac{\partial Q}{\partial t} + \mathrm{v}\frac{dQ}{dr} = \mathrm{v}\frac{dQ}{dr}. \tag{2.14}$$

We therefore calculate dQ/dr from the time dependent solution using

$$\frac{dQ}{dr} = \frac{\Lambda(r)}{\mathrm{v}(r)}, \tag{2.15}$$

where $\mathrm{v}(r)$ is the wind velocity at each point in the heating shell from the time-dependent solution. The problem with this is that at the inner edge of the heating shell the heating rate is finite while the velocity is very close to zero, resulting in a slight overestimate of the total energy input near the inner edge of the shell in the steady wind solution. Care must also be taken in integrating through the singular point in equation (2.11) at $M^2 = 1$. Most authors (e.g. Lamers and Cassinelli 1999) solve the steady wind equations starting from this point but for our purposes it is better to start the integration outside of the heating shell where the energy is well determined. We integrate through the critical point by using a first order Taylor expansion and appropriate limit(s), although this introduces a small discrepancy between the steady state and time-dependent results in this region (Figure 2.5).

Having determined the energy and heating gradient at each point in the wind we integrate (2.11) both inwards and outwards from the chosen point above the heating shell using a fourth order Runge-Kutta integrator (scaling (2.11) to the units described in §2.2.1). The velocity profile is then given by $\mathrm{v}^2 = M^2 c_s^2$ where

$$c_s^2(r) = \frac{2(\gamma-1)}{2+M^2(r)(\gamma-1)}\left[e(r) + \frac{GM}{r}\right]. \tag{2.16}$$

The resulting steady wind solution is shown in Figure 2.5 along with the time-dependent solution. The two profiles are in excellent agreement, proving the validity of our time-dependent numerical solution and the assumption that the wind is in a steady state. The steady solution thus provides an accurate estimate of the velocity at arbitrarily large radii (although as pointed out previously this is set by the value of the steady state Bernoulli energy).

2.2.6 Terminal wind velocities as a function of heating rate

Using the steady wind extrapolation of the time-dependent solution, we can determine the relationship between the heating rate and the terminal wind velocities. In order to make a useful comparison between the heating rates used in both the Newtonian and the relativistic regimes, we need to define a local canonical heating rate $\Lambda_c(r)$ valid in both sets of regimes. In dimensional terms the heating rate $\Lambda(r)$ corresponds to an input energy per unit mass per unit time. Thus we need to define the local canonical heating rate as

$$\Lambda_c(r) = \frac{\Delta E}{\Delta t}, \tag{2.17}$$

for some relevant energy ΔE and some relevant timescale Δt.

Although there are many different ways in which we might define a canonical heating rate, we find that the results are not sensitive to the particular choice made. Ideally we wish to choose a heating rate which reflects the physical processes inherent in the jet acceleration process. Although these processes remain obscure, the fundamental source of the energy available for jet acceleration is the rotational

energy present in the accretion disc. For this reason we take the canonical energy per unit mass, ΔE, to be the energy released locally by bringing to rest a particle of unit mass which is orbiting in a circular orbit at radius r. In the Newtonian regime this is simply the kinetic energy of a circular orbit

$$\Delta E = \frac{1}{2}\mathrm{v}_\phi^2 = \frac{GM}{2r}. \tag{2.18}$$

(An alternative possibility, for example, would be to take ΔE to be the energy released by dropping a particle from infinity and bringing it to rest at radius r, which would correspond to the escape energy from that radius, GM/r.) By similar reasoning, we take the canonical timescale on which the energy is released to be the orbital timescale at radius r, that is $\Delta t = \Omega_o^{-1}$, where

$$\Omega_o = (GM/r^3)^{1/2}. \tag{2.19}$$

Using this, the local canonical heating rate is given by

$$\Lambda_c(r) = \Delta E \times \Omega_o = \frac{(GM)^{3/2}}{2r^{5/2}}. \tag{2.20}$$

This definition of a local canonical heating rate thus enables a direct comparison between the results of the Newtonian and relativistic calculations. In practice we must take an appropriate average heating rate $\langle\Lambda\rangle$ in each case since heat is added over a range of radii. We average across the volume of the heating shell, using

$$\langle\Lambda\rangle = \frac{\int_{r_1}^{r_2}\Lambda(r)r^2dr}{\Lambda_c(r_{\max})\int_{r_1}^{r_2}r^2dr}, \tag{2.21}$$

where $r_{\max}$ is the radius at which the heating rate $\Lambda(r)$ takes its maximum value and r_1 and r_2 are the lower and upper bounds of the heating shell respectively.

The relation between this average dimensionless heating rate $\langle\Lambda\rangle$ and the terminal wind velocity is shown in Figure 2.6. The wind velocities are plotted in units of the escape velocity $\mathrm{v}_{\mathrm{esc}}$ at R_* and solutions are computed for wind velocities of up to $\sim 3\mathrm{v}_{\mathrm{esc}}$. The important point in the present analysis is that the heating rate can be meaningfully compared to the relativistic results (see below).

2.3 Relativistic jets

Having determined the heating rates required to produce the observed velocities in YSO jets we wish to perform exactly the same calculation within a relativistic framework. We proceed in precisely the same manner as in the non-relativistic case. We adopt the usual convention that Greek indices run over the four dimensions 0,1,2,3 while Latin indices run over the three spatial dimensions 1,2,3. Repeated indices imply a summation and a semicolon refers to the covariant derivative. The density ρ refers to the rest mass density only, that is $\rho = nm_0$ where n is the number density of baryons and m_0 is the mass per baryon.

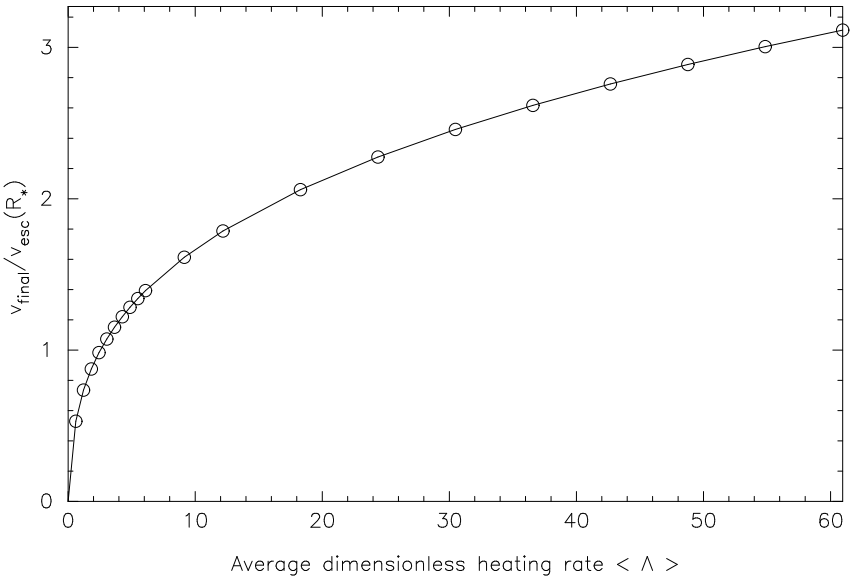

Figure 2.6: Terminal wind velocities plotted as a function of the average dimensionless heating rate $\langle\Lambda\rangle$. Wind velocities are plotted in units of the escape velocity at the inner radius (ie. $r = R_* = 1$), $v_{esc} = (2GM/R_*)^{1/2}$. We compute solutions corresponding to velocities typically observed in YSO jets (with a fairly generous upper limit of $v/v_{esc} \sim 3$).

2.3.1 Fluid equations

The equations describing a relativistic fluid are derived from the conservation of baryon number,

$$(\rho U^{\mu})_{;\mu} = 0, \tag{2.22}$$

the conservation of energy-momentum projected along a direction perpendicular to the four velocity U^{μ} (which gives the equation of motion),

$$h_{\mu\alpha}T^{\alpha\nu}{}_{;\nu} = (g_{\mu\alpha} + U_{\mu}U_{\alpha})T^{\alpha\nu}{}_{;\nu} = 0, \tag{2.23}$$

and projected in the direction of the four-velocity (which gives the energy equation),

$$U_{\alpha}T^{\alpha\nu}{}_{;\nu} = 0. \tag{2.24}$$

Here the quantity $T^{\mu\nu}$ is the energy momentum tensor, which for a perfect fluid is given by

$$c^2 T^{\mu\nu} = \rho h U^{\mu}U^{\nu} + P g^{\mu\nu}, \tag{2.25}$$

where h is the specific enthalpy,

$$h = c^2 + u + \frac{P}{\rho} = c^2 + \frac{\gamma P}{(\gamma - 1)\rho}. \tag{2.26}$$

As in the non-relativistic case u is the internal energy per unit mass, P is the gas pressure and we have used the equation of state given by equation (2.5). The energy equation may also be derived from the first law of thermodynamics using equation (2.22), which is a more convenient way of deriving an energy

equation in terms of the internal energy (rather than the total energy) and in this case ensures that the meaning of the heating term is clear. The metric tensor is given by the Schwarzschild (exterior) solution to Einstein's equations, that is

$$ds^2 = -c^2 d\tau^2 = -\left(1-\frac{2GM}{c^2 r}\right)c^2 dt^2 + \left(1-\frac{2GM}{c^2 r}\right)^{-1} dr^2 + r^2(d\theta^2 + \sin^2\theta d\phi^2). \tag{2.27}$$

We consider radial flow such that $U^\theta = U^\phi = 0$. The four velocity is normalised such that

$$U_\mu U^\mu = -c^2, \tag{2.28}$$

and we define

$$U^t \equiv \frac{dt}{d\tau} = \left(1-\frac{2GM}{c^2 r}\right)^{-1}\left[\left(1-\frac{2GM}{c^2 r}\right) + \frac{(U^r)^2}{c^2}\right]^{1/2}, \tag{2.29}$$

which we denote as

$$U^t = \frac{\Gamma}{\alpha^2} \tag{2.30}$$

where we set for convenience

$$\Gamma = \left[\left(1-\frac{2GM}{c^2 r}\right) + \frac{(U^r)^2}{c^2}\right]^{1/2}, \tag{2.31}$$

and

$$\alpha^2 = \left(1-\frac{2GM}{c^2 r}\right). \tag{2.32}$$

Note that while α corresponds to the lapse function in the $3+1$ formulation of general relativity, the quantity Γ is *not* the Lorentz factor of the gas (which we denote as W) as it is usually defined in numerical relativity (e.g. Banyuls et al. 1997) but is related to it by $W = \Gamma/\alpha$. From (2.29) we also have the relation

$$\frac{\partial U^t}{\partial t} = \frac{U^r}{\alpha^2 \Gamma c^2}\frac{\partial U^r}{\partial t} \tag{2.33}$$

From (2.22), (2.23) and (2.24) using (2.25), (2.27), (2.29) and (2.33) we thus derive the continuity equation,

$$\frac{\partial \rho}{\partial t} + \mathrm{v}^r \frac{\partial \rho}{\partial r} + \frac{\alpha^2 \rho}{\Gamma}\left[\frac{1}{r^2}\frac{\partial}{\partial r}(r^2 U^r) + \frac{U^r}{\alpha^2 \Gamma c^2}\frac{\partial U^r}{\partial t}\right] = 0, \tag{2.34}$$

the equation of motion,

$$\frac{\partial U^r}{\partial t} + \mathrm{v}^r \frac{\partial U^r}{\partial r} + \frac{\Gamma \alpha^2 c^2}{\rho h}\frac{\partial P}{\partial r} + \frac{U^r}{\rho h}\frac{\partial P}{\partial t} + \frac{\alpha^2}{\Gamma}\frac{GM}{r^2} = 0, \tag{2.35}$$

and the internal energy equation,

$$\frac{\partial(\rho u)}{\partial t}+\mathrm{v}^r\frac{\partial(\rho u)}{\partial r}+\frac{\alpha^2}{\Gamma}(P+\rho u)\left[\frac{1}{r^2}\frac{\partial}{\partial r}(r^2U^r)+\frac{U^r}{\alpha^2\Gamma c^2}\frac{\partial U^r}{\partial t}\right]=\frac{\alpha^2}{\Gamma}\rho\Lambda, \tag{2.36}$$

where

$$\mathrm{v}^r\equiv\frac{U^r}{U^t}\equiv\frac{dr}{dt} \tag{2.37}$$

is the velocity in the co-ordinate basis. We define the heating rate per unit mass as

$$\Lambda\equiv T\frac{ds}{d\tau}, \tag{2.38}$$

where T is the temperature, s is the specific entropy and $d\tau$ refers to the local proper time interval (Λ is therefore a local rate of energy input, caused by local physics). A comparison of (2.34), (2.35) and (2.36) with their non-relativistic counterparts (2.1), (2.2) and (2.3) shows that they reduce to the non-relativistic expressions in the limit as $c\to\infty$, and to special relativity as $M\to 0$.

The 'source terms' containing time derivatives of U^r and P are then eliminated between the three equations using the equation of state (2.5) to relate pressure and internal energy. Substituting for pressure in (2.36) and substituting this into (2.35) we obtain the equation of motion in terms of known variables,

$$\frac{\partial U^r}{\partial t}+\frac{\mathrm{v}^r}{X}\left(1-\frac{\gamma P}{\rho h}\right)\frac{\partial U^r}{\partial r}=-\frac{c^2\alpha^4}{\rho h\Gamma X}\frac{\partial P}{\partial r}-\frac{\alpha^2}{\Gamma X}\frac{GM}{r^2}+\frac{\mathrm{v}^r}{X}\frac{\gamma P}{\rho h}\frac{2U^r}{r}-\frac{\mathrm{v}^r}{hX}(\gamma-1)\Lambda, \tag{2.39}$$

where for convenience we define

$$X\equiv 1-\left(\frac{\gamma P}{\rho h}\right)\frac{U^rU^r}{\Gamma^2c^2}, \tag{2.40}$$

and we have expanded the $\frac{1}{r^2}\frac{\partial}{\partial r}(r^2U^r)$ terms in order to combine the spatial derivatives of U^r into one term. We then substitute (2.39) into (2.34) and (2.36) to obtain equations for the density

$$\frac{\partial\rho}{\partial t}+\mathrm{v}^r\frac{\partial\rho}{\partial r}=-\frac{\alpha^2}{\Gamma}\left[\rho A-\frac{\mathrm{v}^r}{h\Gamma X}\frac{\partial P}{\partial r}-\frac{U^rU^r}{\Gamma^2c^2X}\frac{(\gamma-1)}{h}\rho\Lambda\right], \tag{2.41}$$

and internal energy,

$$\frac{\partial(\rho u)}{\partial t}+\mathrm{v}^r\left(1-\frac{\gamma P}{\rho h}\frac{\alpha^2}{\Gamma^2X}\right)\frac{\partial(\rho u)}{\partial r}=-\frac{\alpha^2}{\Gamma}\left[(P+\rho u)A-\left(1+\frac{U^rU^r}{\Gamma^2c^2X}\frac{\gamma P}{\rho h}\right)\rho\Lambda\right]. \tag{2.42}$$

where for convenience we have defined

$$A\equiv\left[1-\frac{U^rU^r}{\Gamma^2c^2X}\left(1-\frac{\gamma P}{\rho h}\right)\right]\frac{\partial U^r}{\partial r}+\left[1+\frac{U^rU^r}{\Gamma^2c^2X}\left(\frac{\gamma P}{\rho h}\right)\right]\frac{2U^r}{r}-\frac{U^r}{\Gamma^2c^2X}\frac{GM}{r^2} \tag{2.43}$$

From the solution specifying U^r we calculate the velocity measured by an observer at rest with respect

to the time slice (referred to as *Eulerian* observers), which is given by

$$\overline{\mathrm{v}}^r = \frac{U^r}{\alpha U^t} = \frac{\mathrm{v}^r}{\alpha}, \tag{2.44}$$

since there are no off-diagonal terms (ie. zero shift vector) in the Schwarzschild solution. For these observers the Lorentz factor is given by

$$W = \left(1 - \frac{\overline{\mathrm{v}}^r \overline{\mathrm{v}}_r}{c^2}\right)^{-1/2}, \tag{2.45}$$

where $\overline{\mathrm{v}}^r \overline{\mathrm{v}}_r = g_{rr} \overline{\mathrm{v}}^r \overline{\mathrm{v}}^r$, such that $U^r = W \overline{\mathrm{v}}^r$.

2.3.2 Scaling

The usual practice in numerical relativity is to scale in so-called geometric units such that $G = M = c = 1$. In these units the length scale would be the geometric radius GM/c^2 and the velocity would have units of c. Instead for the current problem, we adopt a scaling analogous to that of the non-relativistic case, that is we choose the length scale to be the radius of the central object, R_*, where R_* is given as some multiple of the geometric radius, ie.

$$[L] = R_* = n\frac{GM_*}{c^2}, \tag{2.46}$$

with $n \geq 2.0$. The mass scale is again the central object mass $[M] = M_*$ and the timescale is given by

$$[\tau] = \left(\frac{GM_*}{R_*^3}\right)^{-1/2} = n^{3/2}\frac{GM_*}{c^3} \tag{2.47}$$

In these units, velocity is measured in units of $[\mathrm{v}] = n^{-1/2}c$ (or equivalently $c^2 = n$). The scaled equations are thus given simply by setting $G = M = 1$ and $c^2 = n$ everywhere.

This scaling ensures that the relativistic terms tend to zero when c (or n) is large and that the numerical values of ρ, ρu and U^r are of order unity. We thus specify the degree to which the gravity/gas dynamics is relativistic by specifying the value of n (*i.e.* the proximity of the innermost radius, and thus the heating, to the Schwarzschild radius, $R_{\mathrm{Sch}} = 2GM/c^2$). We compute solutions corresponding to gas very close to a black hole (highly relativistic, $n = 2.0$, or $R_* = R_{\mathrm{Sch}}$), neutron star (moderately relativistic, $n = 5$, or $R_* = R_{\mathrm{NS}} = 5GM/c^2$, which is equivalent to heating further out and over a wider region around a black hole) and white dwarf/non-relativistic star (essentially non-relativistic, $n = 5000$, or $R_* = 2500R_{\mathrm{Sch}}$). Note that in the highly relativistic case although we scale the solution to $n = 2.0$ such that the mass, length and time scales (and therefore the units of heating rate, energy etc.) correspond to those at $r = R_{\mathrm{Sch}}$, our numerical grid cannot begin at R_* as it does in the other cases. We therefore set the lower bound on the radial grid to slightly below the heating shell (typically $r = 1.01R_*$ where the heating begins at $1.1R_*$). Note that the above scaling is merely to ensure that the numerical solution is of order unity, since we scale in terms of dimensionless variables to compare with the non-relativistic solution.

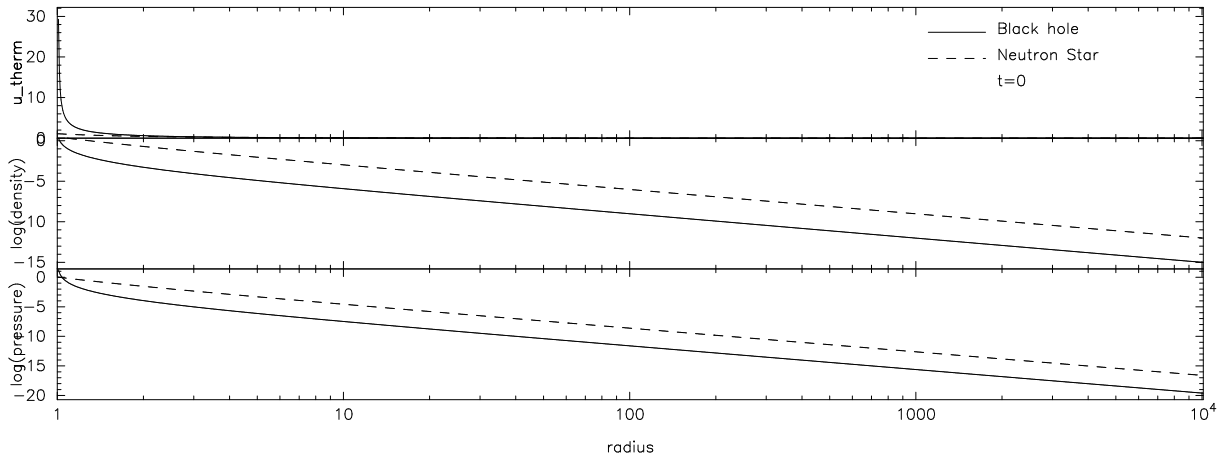

Figure 2.7: The initial conditions for the gas reservoir for the relativistic cases of a neutron star (dashed line) ($R_*/R_{\rm Sch} = 2.5$) and black hole (solid line)($R_*/R_{\rm Sch} = 1.0$). Note, however, that the innermost radius is at $r = 1.01R_*$ in the latter case. We plot profiles of internal energy per unit mass (or temperature), density and pressure, as functions of radius. These quantities are given in units of GM/R_*, M/R_*^3 and $M_*/(R_*t_*^2)$ respectively. Note that steeper gradients are required to hold the gas in hydrostatic equilibrium as the gravitational field becomes more relativistic. The black hole reservoir is of lower density than the neutron star version because of the choice of the polytropic constant (chosen such that the central density is of order unity).

2.3.3 Numerical Solution

In order to solve the relativistic fluid equations numerically we use a method analogous to that used in the non-relativistic case (Figure 2.1). That is, we first compute U^r on the staggered (half) grid and use this to solve for ρ and ρu on the integer grid points. Again the advective terms are discretized using upwind differences (where the 'upwindedness' is determined from the sign of the co-ordinate velocity $\mathbf{v}^r$) and other derivatives are calculated using centred differences. As in the non-relativistic case, where a centred difference is used, the quantities multiplying the derivative are interpolated onto the half grid points if necessary. In equation (2.41) we evaluate the $\partial P/\partial r$ term using upwind differences.

2.3.4 Initial Conditions

We determine initial conditions for the relativistic case by setting $U^r = 0$ and $\partial/\partial t = 0$ in (2.39), from which we have

$$\frac{dP}{dr} = -\frac{\rho h}{c^2}\frac{GM}{r^2}\left(1-\frac{2GM}{c^2 r}\right)^{-1}. \tag{2.48}$$

The pressure is thus calculated as a function of ρ, u and P (where $P = (\gamma-1)\rho u$). We solve (2.48) using the same assumptions as in the non-relativistic case (§2.2.3), that is an adiabatic atmosphere such that

$$P = K\rho^\gamma. \tag{2.49}$$

We therefore have

$$\frac{d\rho}{dr} = -\frac{1}{\gamma K\alpha^2}\left[\rho^{(2-\gamma)} + \frac{\gamma K\rho}{c^2(\gamma-1)}\right]\frac{GM}{r^2}, \tag{2.50}$$

which we solve using a first order (Euler) discretization to obtain a density profile. The pressure may then be calculated using (2.49), however to ensure that hydrostatic equilibrium is enforced numerically we solve (2.48) using the same discretization as in the fluid equations, integrating inwards from the outer boundary condition $P(r_{\rm max}) = K\rho(r_{\rm max})^\gamma$. However in this case the pressure gradient also depends on the pressure, so we use the pressure calculated from (2.49) to calculate the initial value of the specific enthalpy h and iterate the solution until converged ($[P^{n+1} - P^n]/P^n < 10^{-10}$). In the black hole case the resulting pressure differs from that found using (2.49) by $\Delta P/P \sim 10^{-2}$. We choose K such that the central density is of order unity – typically we use $K = 10\gamma/(\gamma-1)$ in the black hole case. Note that changing K simply changes the amount of matter present in the atmosphere but does not affect the temperature scaling and does not affect the final results (although it significantly affects the integration time since it determines the strength of the shock front and the amount of mass to be accelerated).

Initial conditions calculated in this manner for the black hole ($R_*/R_{\rm Sch} = n/2 = 1.0$) and neutron star ($R_*/R_{\rm Sch} = 2.5$) atmospheres are shown in Figure 2.7. The initial setup reduces to that of Figure 2.2 in the non-relativistic limit when the same value of K is used. We set the outer boundary at $r/R_* = 10^4$, using 1335 radial grid points (again on a logarithmic grid).

2.3.5 Results

The results of a typical (n=2.0) relativistic simulation are shown in Figure 2.8 at $t = 1000$. Again we observe that the wind structure reaches a quasi-steady state, with the velocity approaching a steady value at large radii. Note that because the steady state density is higher than that of the surrounding medium no wide shock front is observed.

Plotting the mass outflow rate $\dot{M} = 4\pi r^2 \rho U^r$ and the relativistic Bernoulli energy $E_{\rm rel} = \frac{1}{2}\Gamma^2 h^2/c^2 - \frac{1}{2}c^2$ (see e.g. Shapiro and Teukolsky 1983) as a function of radius (Figure 2.9), we see that indeed the structure approaches that of a steady (relativistic) wind (that is, the energy and $\dot{M}$ profiles are flat above the heating zone). We may thus apply a relativistic steady wind solution with this Bernoulli energy as an initial value to determine the final velocity and Lorentz factor as $r \to \infty$. Note that we cannot apply a non-relativistic steady wind solution because although the gravity is non-relativistic, the outflow velocities are not. As in the non-relativistic case the final wind velocity is determined by the steady Bernoulli energy, since in this case as $r \to \infty$, $E_{\rm rel} \to \frac{1}{2}[(U^r)^2 - c^2]$.

2.3.6 Steady wind solution

Relativistic, steady state ($\partial/\partial t = 0$) winds were first studied by Michel (1972) and extended to include energy deposition by Flammang (1982). The problem has recently received attention in the context of neutrino-driven winds in gamma-ray burst models by Pruet et al. (2001) and Thompson et al. (2001). We proceed in a manner analogous to that of the non-relativistic solution. Setting $\partial/\partial t = 0$ the continuity (2.22) and momentum (2.23) equations become

$$\frac{1}{\rho}\frac{\partial \rho}{\partial r} + \frac{1}{U^r}\frac{\partial U^r}{\partial r} + \frac{2}{r} = 0 \tag{2.51}$$

$$U^r \frac{\partial U^r}{\partial r} + \frac{\Gamma^2 c^2}{\rho h}\frac{\partial P}{\partial r} + \frac{GM}{r^2} = 0 \tag{2.52}$$

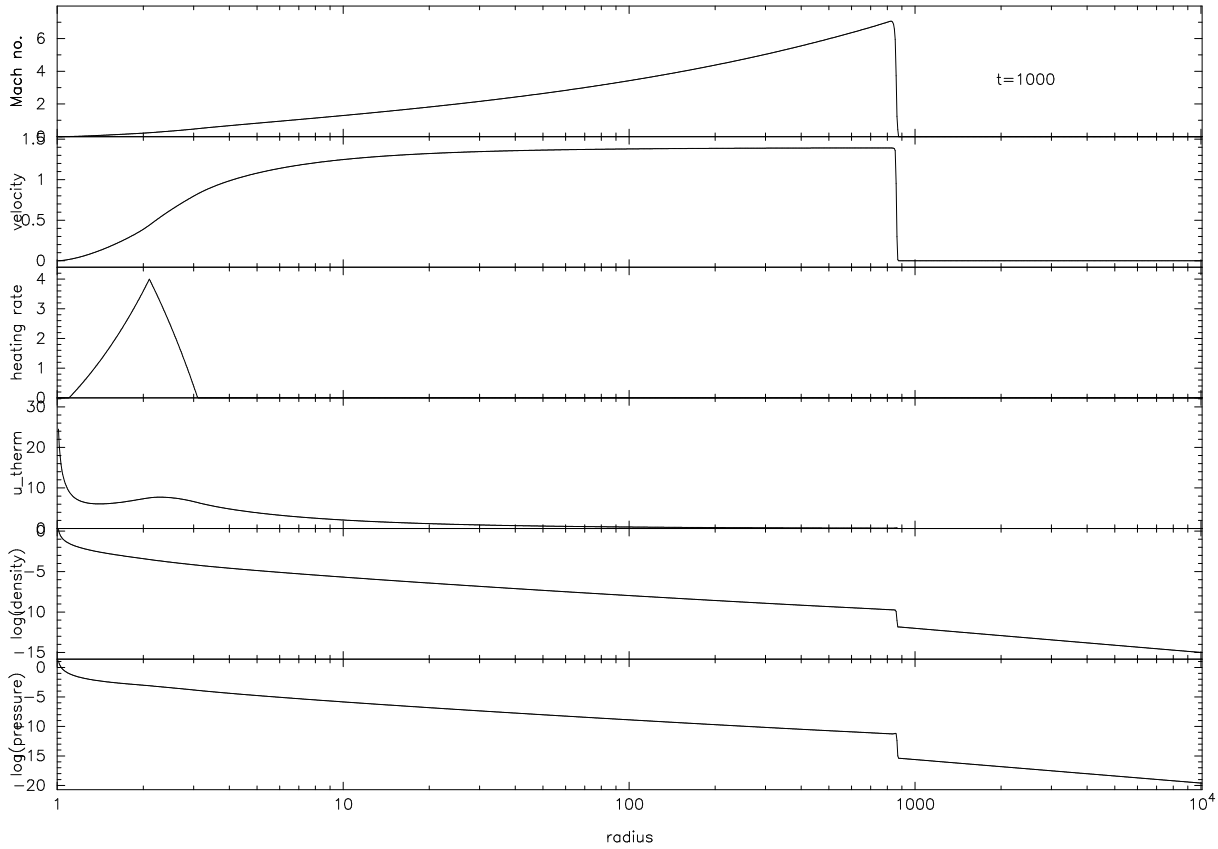

Figure 2.8: Results of a typical black hole relativistic simulation at t=1000 (where units of time are the dynamical time at the central object). Quantities shown are the Mach number (v/c_s), velocity for Eulerian observers ($\bar{v}$), heating rate (Λ), internal energy per unit mass ($u \equiv u_{\rm therm}$), log(density) and log(pressure). Units of velocity are such that $c = \sqrt{2}$ and as in the non-relativistic case energy has units of GM/R_*.

where (2.51) is equivalent to

$$r^2 \rho U^r = \text{const.} \tag{2.53}$$

Combining (2.52) and (2.51) we obtain

$$\frac{1}{U^r}\left[(U^r)^2 - \frac{c^2\Gamma^2 c_s^2}{h\gamma}\right]\frac{\partial U^r}{\partial r} = -\frac{c^2\Gamma^2}{h\gamma}\frac{dc_s^2}{dr} + \frac{c^2\Gamma^2}{h\gamma}\frac{2c_s^2}{r} - \frac{GM}{r^2}, \tag{2.54}$$

where $c_s^2 = \gamma P/\rho$ and $(U^r)^2 \equiv U^r U^r$. From the first law of thermodynamics and (2.52) we derive the relativistic Bernoulli equation in the form

$$\frac{d}{dr}\left(\frac{1}{2}\frac{\Gamma^2 h^2}{c^2}\right) = \frac{h\Gamma^2}{c^2}\frac{dQ}{dr}, \tag{2.55}$$

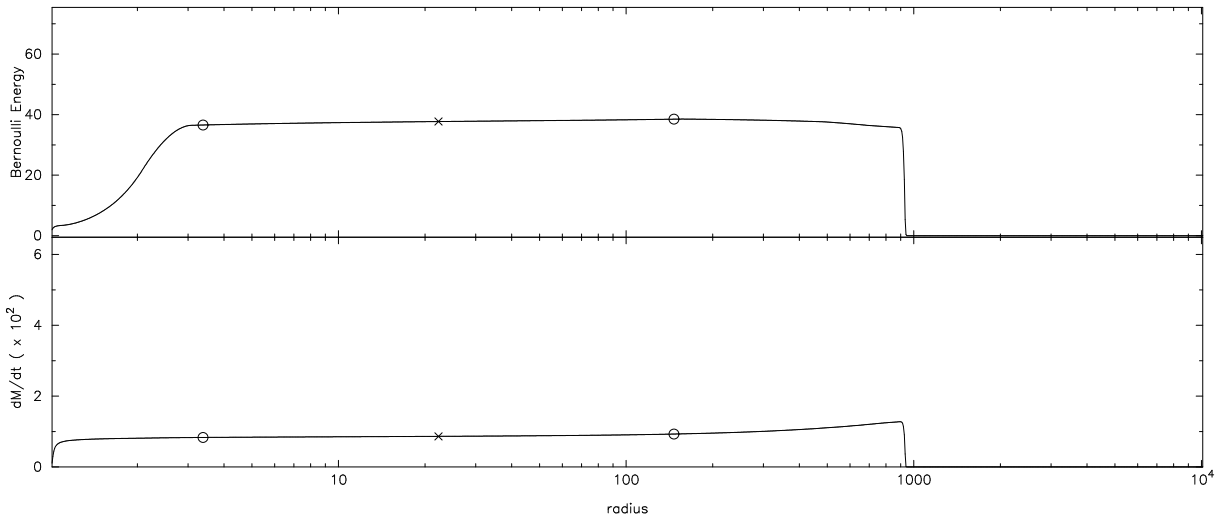

Figure 2.9: The relativistic Bernoulli energy $E_{\rm rel} = \frac{1}{2}\Gamma h/c^2 - \frac{1}{2}c^2$(top) and mass outflow rate $\dot{M} = 4\pi r^2 \rho U^r$ (bottom) in the time-dependent relativistic wind solution with a reasonably high heating rate are shown as functions of radius at time $t = 1000$. In order to match this solution to a steady outflow solution, the Bernoulli energy is assumed to be constant over the region indicated by the two circles, and the steady wind solution is computed using initial values at the point indicated by a cross.

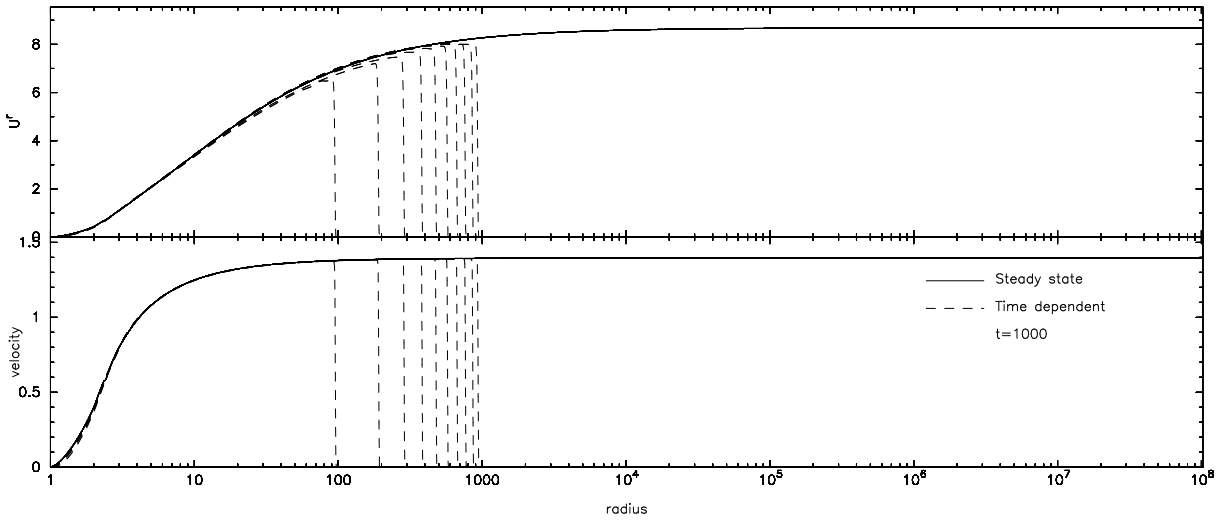

Figure 2.10: The radial profiles of the steady wind r-component of four velocity U^r (top panel) and of the velocity for Eulerian observers $\overline{v}$ (centre panel) are compared to the time-dependent solution (plotted every 100 dynamical times) for a typical relativistic calculation for the black hole (n=2.0) case. Units are such that $c = \sqrt{2}$ on the velocity plots. Note the excellent agreement between the two solutions.

such that both sides reduce to their non-relativistic expressions as $c \to \infty$. The quantity dQ/dr is the local heating gradient as in the non-relativistic case. Expanding this equation we find

$$\frac{dc_s^2}{dr} = (\gamma - 1)\left[\frac{dQ}{dr} - \frac{h}{c^2\Gamma^2}\frac{d}{dr}\left(\frac{1}{2}(U^r)^2\right) - \frac{h}{c^2\Gamma^2}\frac{GM}{r^2}\right]. \tag{2.56}$$

Combining (2.56) and (2.54) and manipulating terms, we obtain an equation for $(U^r)^2$,

$$\frac{d}{dr}(U^r)^2 = \frac{2(U^r)^2}{[(U^r)^2 - c^2\Gamma^2 c_s^2/h]}\left[\frac{c^2\Gamma^2}{h}\frac{2c_s^2}{r} - (\gamma-1)\frac{c^2\Gamma}{h}\left(\Gamma\frac{dQ}{dr}\right) - \frac{GM}{r^2}\right], \tag{2.57}$$

where c_s^2 and $h = c^2 + c_s^2/(\gamma-1)$ are given functions of known variables by integration of the Bernoulli equation (2.55), in the form

$$\frac{d}{dr}(\Gamma h) = \Gamma\frac{dQ}{dr}, \tag{2.58}$$

to ensure that h does not appear in the heating term on the right hand side. The integration is then

$$e(r) = \Gamma h = e(r_\infty) - \int_r^{r_\infty}\left\{\Gamma\frac{dQ}{dr}\right\}dr, \tag{2.59}$$

and hence

$$h = \frac{e(r)}{\Gamma}, \quad c_s^2 = (\gamma-1)(h-c^2). \tag{2.60}$$

The 'heating gradient', $\Gamma dQ/dr$, is calculated from the time-dependent solution using

$$\Gamma\frac{dQ}{dr}(r) = \frac{\alpha(r)\Lambda(r)}{\bar{v}(r)}, \tag{2.61}$$

since

$$\Lambda \equiv T\frac{ds}{d\tau} \equiv \frac{dQ}{d\tau} = U^t\left(\frac{\partial Q}{\partial t} + v^r\frac{dQ}{dr}\right), \tag{2.62}$$

where τ is the proper time and $U^t = \Gamma/\alpha^2$. The velocity profile for an Eulerian observer is then calculated using (2.44) and the final Lorentz factor W_∞ using equation (2.45). As in the non-relativistic case we choose a starting point for the integration above the heating shell and integrate outwards from this point using a fourth order Runge-Kutta integrator in order to determine the terminal Lorentz factor. The inward integration (and thus the determination of the steady state heating gradient $\Gamma dQ/dr$) is computed only for consistency. We integrate through the singular point in equation (2.57) by taking a low order integration with larger steps as this point is approached.

The solution calculated using (2.57) is shown in Figure 2.10 plotted against the evolving time-dependent solution. The profiles are in excellent agreement, verifying the accuracy of the relativistic calculation and showing that the wind may indeed be described by the steady state solution.

2.3.7 Terminal wind velocities and Lorentz factors as a function of heating rate

In order to compare the relativistic results to those in the Newtonian regime, we define the local canonical heating rate in a similar manner to the non-relativistic case, that is

$$\Lambda_c(r) = \frac{\Delta E}{\Delta t}, \tag{2.63}$$

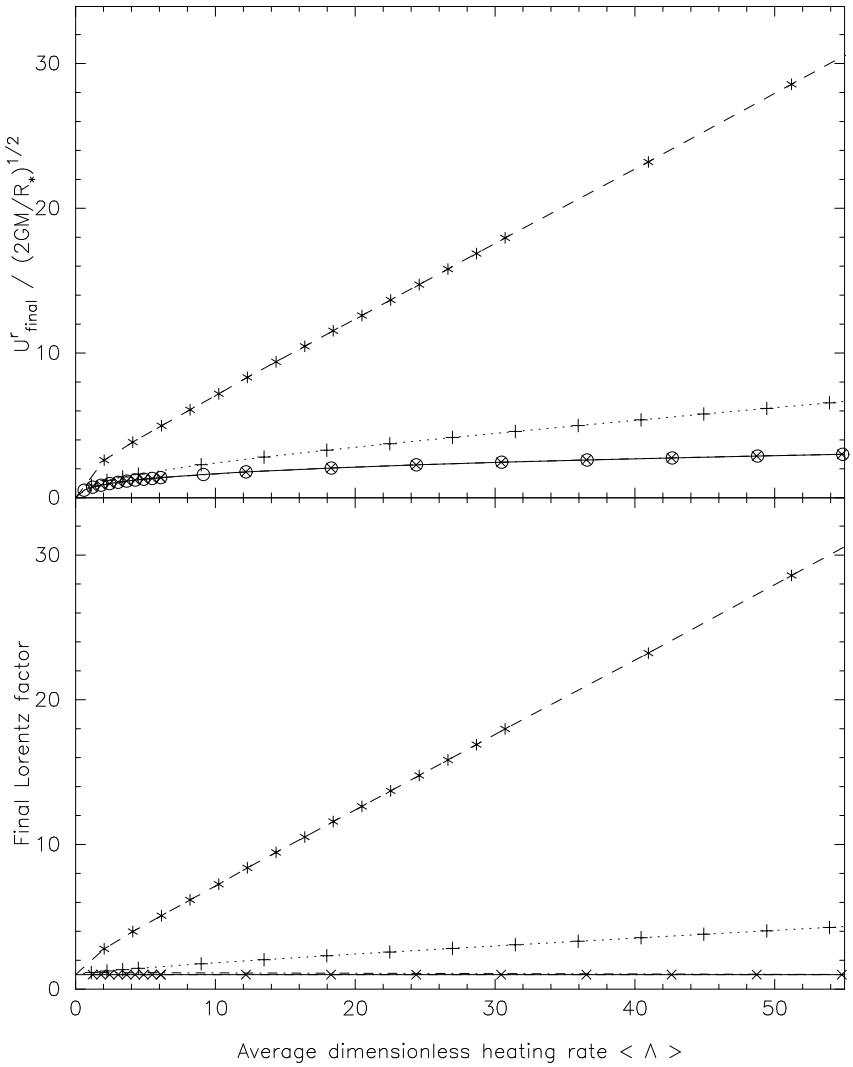

Figure 2.11: The terminal r-component of four velocity U^r (top panel) and Lorentz factor (bottom panel) of the wind in the non-relativistic ($\circ$, solid), white dwarf ($\times$, dot-dashed), neutron star ($+$, dotted) and black hole ($*$, dashed) cases, is plotted as a function of the dimensionless heating rate defined in §2.2.6. The top panel may be compared with Figure 2.6 in the non-relativistic case.

for some relevant energy ΔE and some relevant timescale Δt. As in Section 2.2.6 we take the canonical energy per unit mass, ΔE, to be the energy released locally by bringing to rest a particle of unit mass which is orbiting in a circular orbit at radius r. For a particle orbiting in the Schwarzschild metric this is the difference, ΔE, between the energy constants (defined by the timelike Killing vector) of a circular geodesic at radius r, and a radial geodesic with zero velocity at radius r. This implies (see, for example, Schutz 1985, Chapter 11)

$$\Delta E/c^2 = \frac{1-2GM/rc^2}{[1-3GM/rc^2]^{1/2}} - [1-2GM/rc^2]^{1/2}. \tag{2.64}$$

In the Newtonian limit, this reduces to the expected value $\Delta E = \frac{1}{2}v_\phi^2 = GM/2r$. We again take the canonical timescale on which the energy is released to be the orbital timescale at radius r as measured by a local stationary observer. For a circular geodesic in the Schwarzschild metric, the azimuthal velocity is

given in terms of coordinate time, t, by

$$d\phi/dt = \Omega = (GM/r^3)^{1/2}. \tag{2.65}$$

This is the same expression as for the angular velocity of an orbiting particle in the Newtonian limit. But in terms of the proper time, τ, of a local stationary observer we have, from the metric,

$$d\tau/dt = (1 - 2GM/rc^2)^{1/2}, \tag{2.66}$$

and thus $d\phi/d\tau = \Omega_o$, where

$$\Omega_o^2 = \frac{GM}{r^3}\left[1 - \frac{2GM}{rc^2}\right]^{-1}. \tag{2.67}$$

Using this, the local canonical heating rate is therefore given by

$$\Lambda_c = \Delta E \times \Omega_o. \tag{2.68}$$

In the Newtonian limit, $r \gg 2GM/c^2$, this becomes as expected $\Lambda_c \simeq (GM)^{3/2}/2r^{5/2}$. As in the non-relativistic case we use the canonical heating rate derived above to define a dimensionless heating rate $\langle\Lambda\rangle$ as an appropriate volume average using equation (2.21).

The final Lorentz factor of the wind plotted as a function of this dimensionless heating rate is given in the bottom panel of Figure 2.11 in the highly relativistic (black hole), moderately relativistic (neutron star, equivalent to a broader heating shell further away from a black hole) and non-relativistic (white dwarf) cases.

We would also like to make a meaningful comparison of the final wind velocities in units of the escape velocity from the star. Note that we cannot simply compare the scaled velocities since we are in effect introducing a 'speed limit' in the relativistic solution such that the (scaled) relativistic velocity will always be slower than in the equivalent non-relativistic solution. Rather, we compare the 'momentum per unit mass', which in the relativistic case is given by the four velocity $U^r = dr/d\tau$ (in special relativity this is given by $U^r = \gamma v^r$, where γ is the Lorentz factor). Scaling this in units of the (Newtonian) escape velocity from the central object $(2GM/R_*)^{1/2}$ we can make a useful comparison with the non-relativistic results in terms of the actual energy input. This velocity is plotted in the top panel of Figure 2.11 against the dimensionless heating rate and is clearly higher in the relativistic case. The non-relativistic results correspond to those shown in Figure 2.6.

2.4 Discussion and Conclusions

In this chapter we have considered the injection of energy at a fixed radius into an initially hydrostatic atmosphere as a simple model of the acceleration process in both non-relativistic and relativistic jets. The problem is inherently time-dependent since the velocity is zero at the base of the atmosphere. We have therefore used time-dependent gas dynamics. In order to determine the terminal velocity of the resulting outflow we have used the fact that if the mass in the outflow is small compared to the initial mass reservoir then the outflow will reach an approximate steady state. Once the gas in the time-dependent solution has

evolved to a sufficiently large radius we are therefore able to match the solution to a steady-state wind profile (with a heating term) in order to determine the solution at infinity. The resulting terminal velocities and corresponding Lorentz factors are shown in Figures 2.6 and 2.11.

The first point to note, from the top panel of Figure 2.11 is that the dimensionless energy (or momentum) imparted to the gas is clearly larger in the relativistic case. The resulting outflow velocities also scale linearly with heating rate in this case, whereas in the non-relativistic case the relative increase in the outflow velocity becomes smaller as the heating rate becomes larger. These effects can be understood by considering the effect of the relativity in imposing a speed-limit on the gas as it travels through the (fixed) heating shell. In the non-relativistic case, as the gas is accelerated to higher velocities the time spent in the heating zone also becomes smaller, resulting in the tail-off in the terminal velocity with increasing heating rate. In the relativistic case, once the gas has been accelerated to close to the speed of light, the time spent in the heating zone remains constant ($\sim c$) and consequently the total energy imparted to the outflow scales linearly with dimensionless heating rate $\langle\Lambda\rangle$.

From Figure 2.6 we see that a dimensionless heating rate of $\langle\Lambda\rangle \simeq 17$ gives rise to a terminal outflow velocity of $v_{jet} \simeq 2v_{esc}$ in a Newtonian potential. For the same heating rate, in Figure 2.11, we see that the 'neutron star' wind, for which the heating rate peaks at about 5.2 R_{Sch} becomes mildly relativistic ($\gamma_{jet} \sim 2$), whereas the 'black hole' wind, for which the heating rate peaks at about 2.1 R_{Sch}, leads to an outflow with $\gamma_{jet} \simeq 11$. Similarly a dimensionless heating rate of $\langle\Lambda\rangle \simeq 55$ gives rise to a terminal velocity of $v_{jet} \simeq 3v_{esc}$ in the Newtonian case, to an outflow with $\gamma_{jet} \sim 4$ in the mildly relativistic case, and to an outflow with $\gamma_{jet} \simeq 31$ in the strongly relativistic case. We have already noted (§2.2.6) that although the exact numerical values here do depend slightly on the exact definition of the dimensionless heating rate, the basic results remain unchanged. For example, using the Newtonian dimensionless heating rate (§2.2.6) in the strongly relativistic case gives a Lorentz factor of $\gamma_{jet} \simeq 5$ for the rate which corresponds to $v_{jet} \simeq 2v_{esc}$ in the non-relativistic case.

It must be cautioned that this analysis does not assume that all of the physical processes in the jet acceleration process have been properly represented (for example the process by which the energy is transferred from rotational energy in the disk into kinetic energy in the outflow is clearly magnetic in nature), nor that all of these physical processes should be identical between the various classes of jet. It is evident that more detailed physical models need to be developed before further conclusions can be drawn. Nevertheless, the generic nature of the analysis presented in this chapter suggests that some conclusions into the physical processes involved in the jet acceleration process can be drawn.

On the basis of the simple physical models constructed in this chapter, therefore, it seems not unreasonable to suggest that the relativistic jets observed in AGN are simply scaled-up versions of their non-relativistic (YSO) counterparts and that the intrinsic acceleration process is the same in both classes of object. For this to be the case, two further conditions must also hold. The first is that jet acceleration must occur close to the central gravitating object, in order to make use of the speed of light as a limiting velocity in the black hole case. The second is that, since the dimensionless heating rates required are much larger than unity, the energy released in the outflow must be imparted to only a small fraction of the available accreting material.